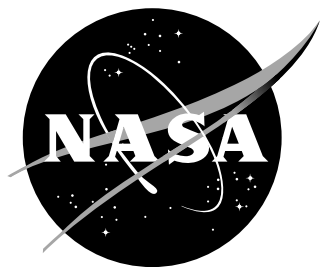NASA/CR–2015–218960

Code-to-Code Comparison, and Material Response Modeling of Stardust and MSL using PATO and FIAT

Ali D. Omidy, Francesco Panerai & Alexandre Martin
University of Kentucky, Lexington, KY 40506

Jean R. Lachaud
University of California Santa Cruz, Moffett Field, CA 94043

Ioana Cozmuta & Nagi N. Mansour
NASA Ames Research Center, Moffett Field, CA 94043

June 2015

Since its founding, NASA has been dedicated to the advancement of aeronautics and space science. The NASA scientific and technical information (STI) program plays a key part in helping NASA maintain this important role.

The NASA STI Program operates under the auspices of the Agency Chief Information Officer. It collects, organizes, provides for archiving, and disseminates NASA's STI. The NASA STI Program provides access to the NTRS Registered and its public interface, the NASA Technical Reports Server, thus providing one of the largest collections of aeronautical and space science STI in the world. Results are published in both non-NASA channels and by NASA in the NASA STI Report Series, which includes the following report types:

- TECHNICAL PUBLICATION. Reports of completed research or a major significant phase of research that present the results of NASA programs and include extensive data or theoretical analysis. Includes compilations of significant scientific and technical data and information deemed to be of continuing reference value. NASA counterpart of peer-reviewed formal professional papers, but having less stringent limitations on manuscript length and extent of graphic presentations.

- TECHNICAL MEMORANDUM. Scientific and technical findings that are preliminary or of specialized interest, e.g., quick release reports, working papers, and bibliographies that contain minimal annotation. Does not contain extensive analysis.

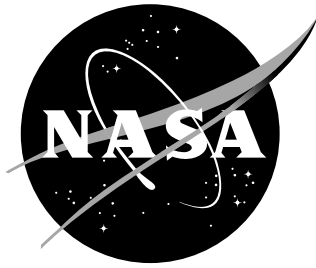- CONTRACTOR REPORT. Scientific and technical findings by NASA-sponsored contractors and grantees.

- CONFERENCE PUBLICATION. Collected papers from scientific and technical conferences, symposia, seminars, or other meetings sponsored or co-sponsored by NASA.

- SPECIAL PUBLICATION. Scientific, technical, or historical information from NASA programs, projects, and missions, often concerned with subjects having substantial public interest.

- TECHNICAL TRANSLATION. English-language translations of foreign scientific and technical material pertinent to NASA's mission.

Specialized services also include organizing and publishing research results, distributing specialized research announcements and feeds, providing information desk and personal search support, and enabling data exchange services.

For more information about the NASA STI Program, see the following:

- Access the NASA STI program home page at *http://www.sti.nasa.gov*

- E-mail your question to help@sti.nasa.gov

- Phone the NASA STI Help Desk at 757-864-9658

- Write to:
  NASA STI Information Desk
  Mail Stop 148
  NASA Langley Research Center
  Hampton, VA 23681–2199

NASA/CR–2015–218960

Code-to-Code Comparison, and Material Response Modeling of Stardust and MSL using PATO and FIAT

Ali D. Omidy, Francesco Panerai & Alexandre Martin
University of Kentucky, Lexington, KY 40506

Jean R. Lachaud
University of California Santa Cruz, Moffett Field, CA 94043

Ioana Cozmuta & Nagi N. Mansour
NASA Ames Research Center, Moffett Field, CA 94043

Acknowledgments

This report is available in electronic form at

http://

Abstract

This report provides a code-to-code comparison between PATO, a recently developed high fidelity material response code, and FIAT, NASA's legacy code for ablation response modeling. The goal is to demonstrates that FIAT and PATO generate the same results when using the same models. Test cases of increasing complexity are used, from both arc-jet testing and flight experiment. When using the exact same physical models, material properties and boundary conditions, the two codes give results that are within 2% of errors. The minor discrepancy is attributed to the inclusion of the gas phase heat capacity (c_p) in the energy equation in PATO, and not in FIAT.

1 Introduction

During atmospheric entry, spacecraft are exposed to high heat fluxes. In order to protect the vehicle from the extreme heating, thermal protection systems (TPS) are used. One of the options for ablative TPS material is a porous, fibrous preform impregnated with a phenolic resin. Through various complex mechanisms, this class of material uses the incoming heat to trigger chemical reactions that will reduce the surface heat flux [1] as well as minimize the transfer of kinetic energy to thermal energy [2, 3]. The *Phenolic Impregnated Carbon Ablator* (PICA) [4] developed by NASA belongs to this class of materials. It successfully flew on various spacecraft such as the *Stardust Sample Return Capsule* [5], SpaceX's *Dragon* spacecraft (PICA-X) [6] and, more recently, the *Mars Science Laboratory* (MSL) entry spacecraft [7] .

Pyrolysizing ablative materials , such as PICA, protect the spacecraft in multiple ways. As more energy is conducted to the surface of the vehicle, the ablator starts to react to the high temperature. First, the phenolic resin within the ablative material begins to pyrolyze and is transformed into char and gas. Then, the charred surface starts to ablate, more often through the oxidation of a thin layer near the surface [8, 9]. As these processes take place, several regions within the ablators can be identified. These regions are illustrated in Figure 1.

The virgin region is located near the substructure, where the resin has yet to receive the amount of energy necessary for chemical reactions to occur. In this region, the phenolic phase, which can be seen in the scanning electron microscope (SEM) image presented in Figure 1, preserves its initial microstructure. The region above the pyrolysis zone is where the chemical decomposition of the phenolic occurs. Despite the fact that pyrolysis of the phenolic has been extensively studied, in the context of light weight ablators, the gas interaction with the fibers complexify the process. Moreover, as the resin is transformed into a gas, it travels freely within the ablator. Although most of the gas will eventually exit at the surface, it may also travel in the virgin region of the material [10, 11]. The gas reacts very differently depending on the local thermodynamic conditions. Specific thermodynamic conditions lead to the creation of the next layer, in which the phenolic gas generates carbon deposition on the fiber. This process is generally known as coking, and creates what is known as the coking region.

The final region, the ablation zone, is located nearest to the outer surface of the TPS. Once the phenolic has been completely transformed into either a pyrolysis gas or coke, only a solid carbon char remains. This solid material is susceptible to further reactions as the surrounding boundary layer gas comes in contact with the carbon as it diffuses into shallow depths of the ablator. The oxygen present within the boundary layer gas reacts with the char, reducing the radius of the fibers and producing carbon oxides. Depending on the conditions experienced, this process can either occur at the surface if it is diffusion limited (surface ablation) or within a thin layer if it is reaction limited (volumetric ablation) [8].
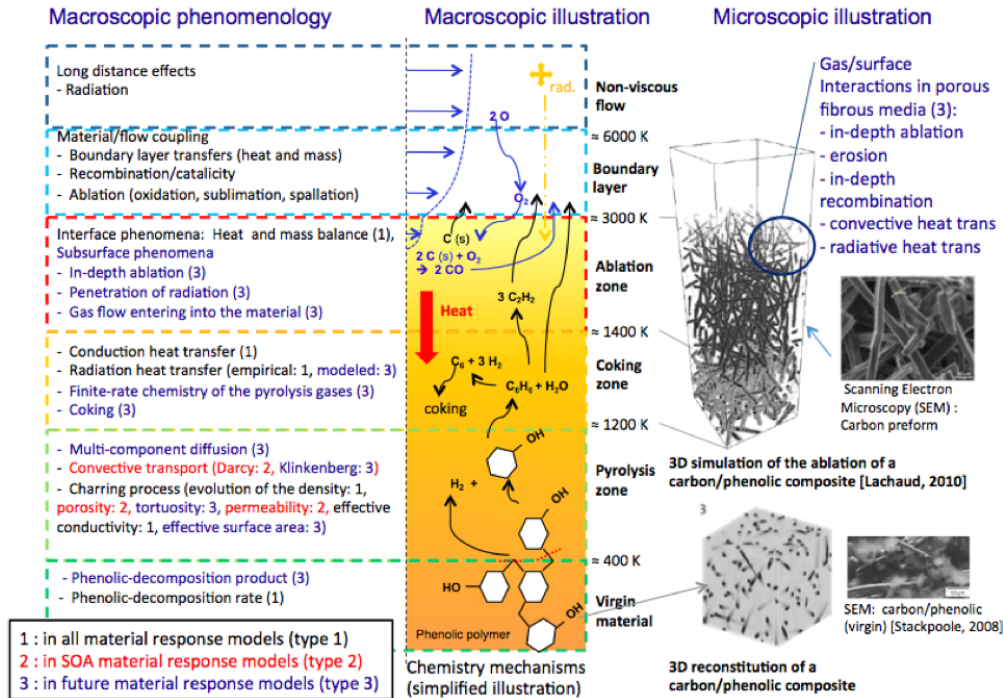
Figure 1. *Detailed zone degradation rendering with microscopic and macroscopic illustrations. Macroscopic phenomenology relating to material response codes are also presented. The incorporation of these phenomena help to dictate the overall material response type (image taken from Ref. [12], with permission).*

As the fibers are further decomposed the structural integrity of the fibers are weakened, allowing shear forces to compromise the fibers, leading to the mechanical removal of the oxidized fibers.

Recently, the high-fidelity material response (MR) code *Porous-Material Analysis Toolbox based on OpenFOAM* (PATO) [12, 13] has been developed in order to model with high fidelity the complex physical phenomena occurring during the ablation process, and account for those phenomena that are not considered in legacy codes such as FIAT. PATO is a fully portable library for OpenFOAM[1], an open-source finite volume computational fluid dynamic (CFD) software released by OpenCFD Limited. The PATO library is specifically designed to have the capability to test innovative physics-based models for reactive porous materials subjected to high-temperature environments. When using the state-of-the-art ablation design module, PATO is equivalent to NASA's heritage MR code FIAT [14], with two exceptions 1) the addition of the momentum equation and 2) the consideration of the gas phase heat capacity in the energy equation. Both of these are not included in FIAT. Although the code has already gone through extensive code-to-code comparison using the Theoretical Ablative Composite for Open Testing (TACOT) [15], it still lacks the benefits of flight comparison using real, validated material models such as PICA.

Therefore, the goal of the present work is not to validate the high-fidelity modeling options of PATO, but to simply demonstrates that FIAT and PATO generate the same

---

[1]The PATO library is not endorsed by OpenCFD Limited, the producer of the OpenFOAM software and owner of the OPENFOAM® and OpenCFD® trademarks. www.openfoam.org/ [retrieved 11 November 2014].

results when using the same models. To do so, this paper presents three cases of increasing complexity that are compared to FIAT solutions as well as to experimental data. The first problem is a test case proposed at the 5th Ablation Workshop [16], but performed using the PICA model instead of the TACOT model. This test case ensures that the basic material response models are equivalent between the two codes. The second case examines the theoretical temperature profile for locations on the Stardust re-entry vehicle (near the stagnation point and on the heat shield flank), using the CFD code Data Parallel Line Relaxation (DPLR) [17] to generate the solution according to the Best Estimated Trajectory (BET) flight conditions. The third problem is similar to the second, but this time, the analysis is performed for the entry of the Mars Science Laboratory (MSL) spacecraft. For this case, the numerical results of PATO and FIAT can also be compared to the thermocouple measurements obtained during entry by the MEDLI suit [18]. The three studies can be summarized as follows:

1. **Ablation Test Case 1**: 1D, fixed wall temperature of 1600 K, no surface recession

2. **Stardust Return Capsule**: 1D analysis of Cores 1 & Core 2

3. **Mars Science Laboratory**: 1D analysis of MISP Plug 2

2 One-dimensional material response comparison

In order to provide a common basis for comparing the two MR codes, and therefore verify PATO's maturity, PATO is reduced to its simplest form (one-dimension, without the use of any high fidelity models). The only difference between the two codes is that PATO considers the pyrolysis gas to travel through the porous material while FIAT assumes that the gas instantaneously reaches the surface. In PATO, the motion of the gas through the material is solved using a steady-state momentum equation that reduces to:

$$\mathbf{v_g} = -\frac{1}{\phi_g \mu} \frac{1 + \beta/p}{1 + F_0} \underline{\underline{K}} \cdot \nabla p \tag{1}$$

In this equation, the permeability, K, is a tensor since lightweight charring ablators are usually anisotropic due to the preferred orientation of the fibers. The Klinkenberg correction factor [12], represented as β, accounts for slip at the scale of the pores. F_0 is the Forchheimer number which accounts for the convective flux, and is only significant at gas velocities higher than 50 m/s [19]. When β and F_0 are neglected, this momentum equation reduces to Darcy's Law, and the gas velocity becomes directly proportional to the gradient in pressure. It is important to point out that the momentum equation is one of the two modeling differences between the two MR codes [12].

The remaining conservation equations, mass and energy, are represented below.

Mass Conservation:

$$\partial_t(\varepsilon_g \rho_g) + \partial_x \cdot (\varepsilon_g \rho_g \mathbf{v_g}) = \Pi \tag{2}$$

Energy Conservation:

$$\partial_t(\rho_a e_a) + \partial_x \cdot (\varepsilon_g \rho_g h_g \mathbf{v_g}) + \partial_x \cdot \sum_{i=1}^{N_g}(h_i \mathbf{F}_i) = \partial_x \cdot (\underline{\underline{k}} \cdot \partial_x T) + \mu \varepsilon_g^2 (\underline{\underline{K}}^{-1} \cdot \mathbf{v}) \cdot \mathbf{v} \tag{3}$$

For all the test-problems discussed here, both codes are run with an adiabatic boundary condition at the bond-line wall, and the results are compared using overall space- and time-averaged error. The temperature values at a specific depth, or TC values, is an efficient means of comparison and is used throughout the study.

This local, time-dependent average error $\epsilon_{x,t}$ is represented by the following:

$$\epsilon_{x,t} = \left| \frac{T_P - T_F}{T_P} \right| \times 100 \tag{4}$$

where, T_P and T_F are the temperature for the two codes ($P = $ PATO, $F = $ FIAT), respectively. The overall error ϵ between the two solutions is obtained by calculating the root mean square of all the spatial errors for each time step and each thermocouple:

$$\epsilon = \sqrt{\frac{1}{n_t} \sum_{t=1}^{n_t} \left[\frac{1}{n_{TC}} \sum_{x=1}^{n_{TC}} \epsilon_{x,t}^2 \right]} \tag{5}$$

where n_{TC} is the number of thermocouples, and n_t the number of time steps.

2.1 Ablation Test Case 1

The Ablation Test Case 1 [15] is a simple one-dimension material response test case that was initially proposed for a global code-to-code comparison. The test case consists of a 5 cm deep sample of lightweight charring ablator material heated to a fixed temperature of 1644 K, maintained for a duration of 1 min. The heating is then stopped, leaving the absorbed energy to continue to propagate through the material for an additional 1 min. Through the full duration of the test, the surface of the sample is exposed to a constant pressure of 1 atm, while the back is assumed to be impermeable and adiabatic. Even though this heating condition would not induce surface ablation, the recession functionality is turned off.

In order to streamline the validation process, the material model used for the validation is PICA (in air) instead of TACOT [15]. The latest PICA version is used, which includes material properties from the FIAT-v3.0.1 release. Both codes, PATO and FIAT-v3.0.1, were run under the same defined parameters to allow a one-to-one comparison. The temperature outputs are presented in Fig. D4.
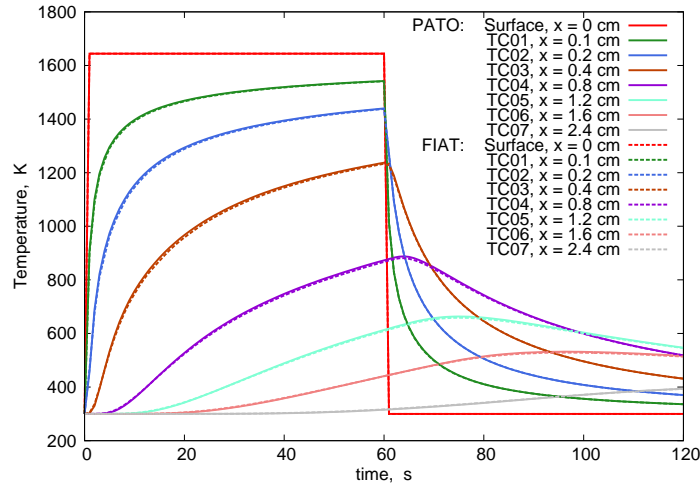

Figure 2. *Ablation test case 1: comparison between PATO and FIAT using PICA. A temperature of 1644 K is applied at the surface for 1 min then remove.*

As expected, both codes provide the anticipated results for the first problem. As the heat propagates into the material the thermocouples near the surface (TC01-03) respond

4

significantly quicker than the deeper thermocouples (TC04-07). As time progresses and the heat source is removed, the temperature equilibrates throughout the material and the thermocouples react accordingly. As can be seen in Fig. D4, PATO and FIAT show good agreement.The root mean square (RMS) error for this case was found to be ϵ of 0.42%.

This first test case gives confidence in the implementation of the PICA material model since previous comparisons between PATO and FIAT using TACOT showed similar trends [12].

2.2 Stardust

One of the most studied ablation cases is the re-entry of the Stardust Sample Return Capsule [5]. With its 12 km/s entry velocity, Stardust still holds the record for fastest entry for a man-made object in earth's atmosphere, and thus provides a stressing case for TPS analysis tool

Due to these extreme re-entry conditions, a high heat pulse was experienced at all locations along the heat shield profile, with maximum heating occurring at the nose of the spacecraft (stagnation point). Unfortunately, the heat shield of the spacecraft was not instrumented, and the only available data was obtained through two extracted heat shield samples (dubbed Core 1 and Core 2). This data, however, is not ideal as the charred ablator was very brittle and was likely damaged at landing. Moreover, modeling efforts have shown that current MR codes significantly over-predict the recession of the TPS [20].

Although stardust was not equipped with thermocouples, in-depth temperature remains the ideal parameter to use for comparison as it is a standard output for any MR code. Figures 3 and 4 show such comparisons between PATO and FIAT, using theoretical thermocouples at half-inch intervals for both extracted cores. The heat flux and pressure at the surface was computed with the CFD solver DPLR, using the Best Estimate Trajectory (BET) [21]. For this second test case, the surface is allowed to ablate. In order to maintain the one-to-one comparison between PATO and FIAT, a fiber failure term (B'_f) is added to PATO to mimic the practice adopted in FIAT. B'_f is defined as a fraction of the non-dimensional surface removal rate B'_c [22].

Core 2 is first analyzed since lower heating rates are expected near the flank of the spacecraft [23], and the conditions are thus closer to the Ablation Test Case 1, previously analyzed. Fig. 3 presents the projected temperature history at each identified thermocouple. Comparing the temperatures at the wall, bond line, and thermocouple locations, an overall RMS error of 0.57% is observed. PATO therefore maintains an excellent agreement with FIAT even when including ablative cases.

Core 1, with results shown in Fig. 4, uses the same initial conditions as Core 2 with a correlating environment map computed from the BET through the use of DPLR. Due to the high heating rate present in the stagnation point region, Core 1 experiences a significantly higher heat flux than Core 2. This condition is enough to generate a small difference in the results, attributed to the inclusion of pyrolysis gas phase heat capacity in the energy equation of PATO. It should also be noted that time and spatial gird convergence errors may also be a contributing factor as these parameters are automatically generated in FIAT, and doesnot offer the possibility to change them through the user interface. As can be seen in Fig. 4, this difference is more notable when considering the first thermocouple. The total error ϵ between the two codes is evaluated at 1.4%.

2.3 Mars Science Laboratory

The atmospheric entry of the MSL spacecraft was of great interest to the scientific community, as the heat shield was equipped with the *MSL Entry, Descent, and Landing Instrumentation* (MEDLI) instrumentation suite [18]. MEDLI was composed of seven surface
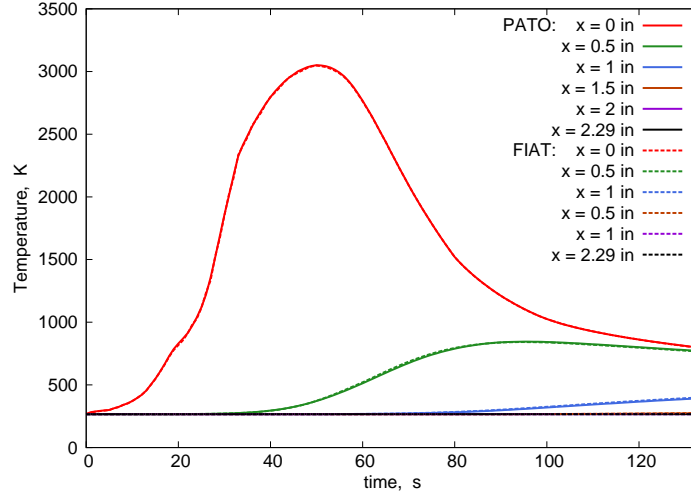
Figure 3. *Stardust test case (Core 2): comparison between PATO and FIAT. Surface heating is applied for the duration of 133 s based upon DPLR.*
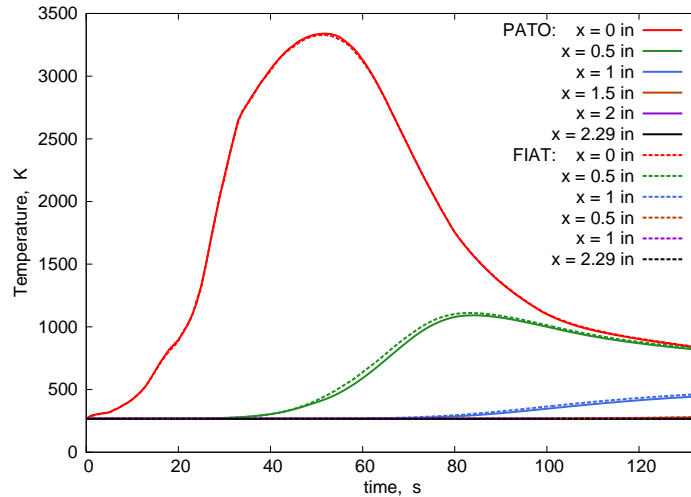
Figure 4. *Stardust test case (Core 1): comparison between PATO and FIAT. Surface heating is applied for the duration of 133 s based upon DPLR.*

pressure transducers, known as *Mars Entry Atmospheric Data System* (MEADS), as well as a combination of seven sets of thermocouples (TC) and a *Hollow aErothermal Ablation and Temperature* (HEAT) sensor, known as the *MEDLI Integrated Sensor Plug* (MISP). Each MISP used four TCs to measure temperature at specific depths within the heat shield, as well as one HEAT sensor to measure the propagation of an isotherm. The location of the MEADS and MISP sensors on the surface of MSL is shown in Figs. 5(a) and 5(b), respectively.

Figures 5(b) and 5(a) also illustrate the expected heat flux as computed with the BET, using the DPLR CFD code [24]. As can be seen on these figures, peak heating occurs near the lower flank, and therefore MISP 2, 3, and 6 experienced higher heat flux than MISP 1 and MISP 4.

As was the case with the Stardust analysis, high heating scenarios cause slight discrepan-
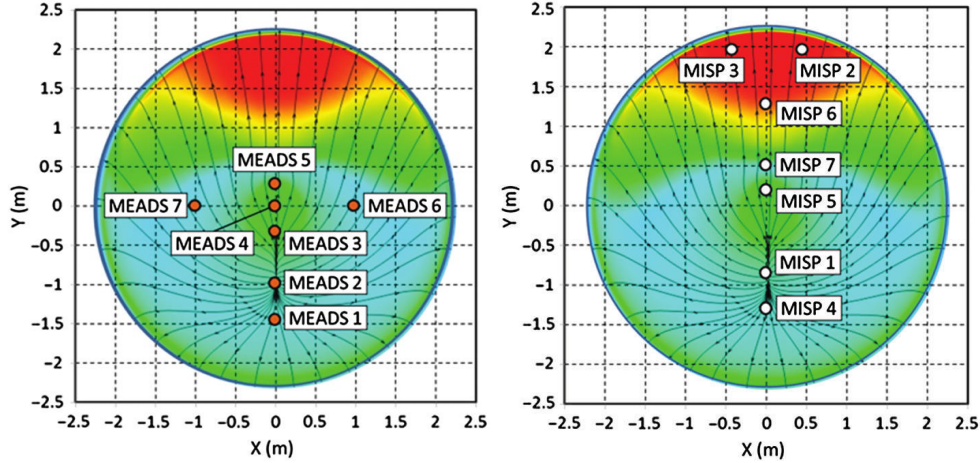
(a) *Location of the MEADS sensors which measure the pressure at the surface of the heat shield. The color contours illustrate heating (image taken from Bose et al. [25], with permission.)*

(b) *Location of the MISP sensors which measure the temperature within the heat shield. The color contours illustrate heating. Image taken from Bose et al. [25].*

Figure 5. *Instrumentation of the heat shield of the Mars Science Laboratory entry spacecraft.*

cies between the results of PATO and FIAT due to the inclusion of the gas phase properties in the energy equation in PATO, but not in FIAT. In order to maximize the potential differences, MISP 2 was selected for the present analysis. All remaining MISPs were also examined in the full study and are presented in the Appendices. For the MSL capsule, the PICA heat shield had a uniform thickness. However, depending on the specific MISP, the depth of thermocouples varies. A detailed list of thermocouple orientation can be obtained from Bose et al. [25]. For MISP 2, the thermocouples are fixed at specified depths of 0.106 in, 0.203 in, 0.456 in, and 0.700 in, respectively. Each MISP was simulated for a duration of 268 s for both PATO and FIAT and then compared to flight measurements from the respective thermocouple. Similar to the Stardust study, the PICA model was used for the material response. To account for the actual composition of Martian atmosphere, a different set of surface themo-chemistry table (B' tables) was implemented.

A comparison of FIAT and PATO's results with the measured temperature data from MISP 2 is presented in Fig. 6 (and in Fig. A8 for the other MISP plugs). Similar to the previous cases, PATO shows good agreement with FIAT, with an average discrepancy of 1.8%. For both codes, the first and second thermocouple burn out within the first 100 s of the capsules entry. Although both codes produce similar results, it is clear from Figure 6 (and Fig. B9) that their results differ from the thermocouples measurements. One reason for this discrepancy is that the current series of tests assumes the back surface of the MISP plug to be adiabatic. In reality, heat is also transferred through the back-face to multiple layers of material, as is the case presented by White et. al [26]which models multiple layers of materials at the back surface. This simplification does explain the discrepancy in the lower TCs and at the end of the simulation, but does not address the discrepancy near the surface, in the early stages of heating.

To investigate the difference between the modeled and measured values, the atmospheric boundary condition is removed from the simulation [27], and the measured values at the nearest surface thermocouple is imposed at the boundary. The results are presented in Fig. 7 (and in Fig. C10 for the other MISP plugs); although the agreement is better, there are still significant differences when comparing the flight data to the simulations.
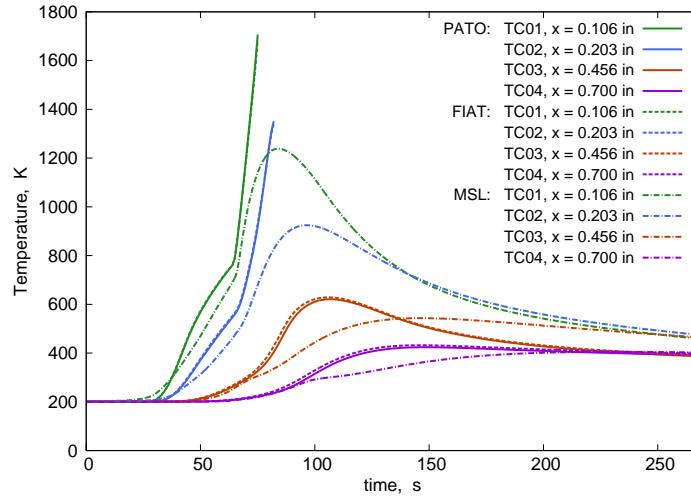
Figure 6. *MISP 2 thermocouple measurements are compared with those of PATO and FIAT. Surface heating for both modeling tools are provided from DPLR, and is applied for a period of 268 s.*
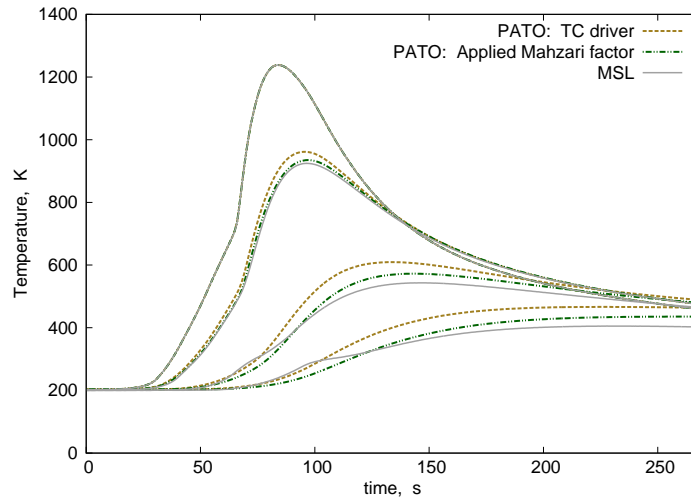
Figure 7. *MISP 2 thermocouple measurements are compared against that of PATO and FIAT. The measure data at the first thermocouple is set as the boundary condition for the duration of the test case and ran for 268 s.*

Recent efforts by Mahzari et al. [27] have recommended factors for both char and virgin thermal conductivity. This study is based upon the uncertainty and sensitivity associated to the location of the thermocouples and the material properties. By implementing these suggested values, represented as the green dotted line in Fig. 7, the models are able to predict values that are significantly closer to flight data. Although these factors increase the accuracy of the models, the "humps" observes in the flight data of the third and fourth TCs are still not captured. However, the nature of this phenomenon is beyond the scope of the present code-to-code comparison.

8

2.4 Summary of results

A summary of the overall errors between the two codes, for all the test cases studied here (including the MSL results presented in Appendix A), is presented in Table D2.

Table 1. *Summary of the overall errors between the PATO and FIAT for all test cases.*

Test Case	ϵ (%)
Ablation Test Case 1	0.42
Stardust – stag. point	1.4
Stardust – Core 1	1.4
Stardust – Core 2	0.57
MSL – MISP 1	0.82
MSL – MISP 2	1.8
MSL – MISP 3	1.9
MSL – MISP 4	0.79
MSL – MISP 5	1.1
MSL – MISP 6	1.8
MSL – MISP 7	1.7

3 Conclusion

High fidelity material response codes, such as PATO, are tools used to analyze the response of a heat shield during atmospheric entry. These tools have the capability to model the complex physical phenomena that occur within the material, such as volumetric ablation and pyrolysis. However, before analyzing the significance of the high fidelity models, the code must be compared to a baseline model. The results of such an exercise are presented here. The test cases modeled showed an excellent agreement with NASA Ames's heritage material response code FIAT. Some test cases exhibited small, almost negligible discrepancies. These were likely due to the inclusion of pyrolysis gas properties in the conservation of energy equation, such as the specific heat and possibly temporal and spatial convergence errors. It was observed that high heat fluxes, and therefore high temperatures, caused greater discrepancies between PATO and FIAT, due to specific heat being directly related to temperature.

References

1. Martin, A. and Boyd, I. D., "Modeling of heat transfer attenuation by ablative gases during the Stardust re-entry," *Journal of Thermophysics and Heat Transfer*, Vol. 29, No. 3, 2015, pp. 450–466,
   doi:10.2514/1.T4202.

2. Amar, A. J., Blackwell, B. F., and Edwards, J. R., "One-Dimensional Ablation Using a Full Newton's Method and Finite Control Volume Procedure," *Journal of Thermophysics and Heat Transfer*, Vol. 22, No. 1, 2008, pp. 72–82,
   doi:10.2514/1.29610.

3. Amar, A. J., Blackwell, B. F., and Edwards, J. R., "Development and Verification of a One-Dimensional Ablation Code Including Pyrolysis Gas Flow," *Journal of Thermophysics and Heat Transfer*, Vol. 23, No. 1, 2009, pp. 59–71,
   doi:10.2514/1.36882.

4. Tran, H. K., Johnson, C. E., Rasky, D. J., Hui, F. C. L., Hsu, M.-T., and Chen, Y. K., "Phenolic Impregnated Carbon Ablators (PICA) for Discovery class missions," in "31st AIAA Thermophysics Conference," New Orleans, LA, AIAA Paper 1996-1911, 1996, pp. 1–14,
doi:10.2514/6.1996-1911.

5. Kontinos, D. A. and Wright, M. J., "Introduction: Atmospheric Entry of the Stardust Sample Return Capsule," *Journal of Spacecraft and Rockets*, Vol. 47, No. 5, 2010, pp. 705–707,
doi:10.2514/1.51522.

6. "SpaceX manufactured heat shield material passes high temperature tests simulating [Press release]," Retreived on November 12, 2014 from http://www.spacex.com/press/2012/12/19/spacex-manufactured-heat-shield-material-passes-high-temperature-tests-simulating, 2009.

7. "Seeing red," *Nature*, Vol. 479, No. 7374, 2011, pp. 446–446,
doi:10.1038/479446a.

8. Lachaud, J. R., Mansour, N. N., Ceballos, A., Pejaković, D., Zhang, L., and Marschall, J., "Validation of a volume-averaged fiber-scale model for the oxidation of a carbon-fiber preform," in "42nd AIAA Thermophysics Conference," Honolulu, HI, AIAA Paper 2011-3640, 2011, pp. 1–10,
doi:10.2514/6.2011-3640.

9. Lachaud, J., Cozmuta, I., and Mansour, N., "Ablation of PICA-like Materials – Surface or Volume phenomenon?" in "6th International Planetary Probe Workshop," Atlanta, GA, 2008. http://hdl.handle.net/1853/26333.

10. Weng, H. and Martin, A., "Numerical Investigation on Charring Ablator Geometric Effects: Study of Stardust Sample Return Capsule Heat Shield," in "53rd AIAA Aerospace Sciences Meeting," Kissimmee, FL, AIAA Paper 2015-0211, 2015, pp. 1–14,
doi:10.2514/6.2015-0211.

11. Weng, H. and Martin, A., "Numerical Investigation of Geometric Effects of Stardust Return Capsule Heat Shield," *Journal of Thermophysics and Heat Transfer*. In preparation.

12. Lachaud, J. and Mansour, N. N., "Porous-Material Analysis Toolbox Based on Open-FOAM and Applications," *Journal of Thermophysics and Heat Transfer*, Vol. 28, No. 2, 2014, pp. 191–202,
doi:10.2514/1.T4262.

13. Lachaud, J., van Eekelen, T., Scoggins, J. B., Magin, T. E., and Mansour, N. N., "Detailed chemical equilibrium model for porous ablative materials," *International Journal of Heat and Mass Transfer*, Vol. 90, 2015, pp. 1034–1045. Doi:10.1016/j.ijheatmasstransfer.2015.05.106.

14. Chen, Y.-K. and Milos, F. S., "Ablation and Thermal Response Program for Spacecraft Heatshield Analysis," *Journal of Spacecraft and Rockets*, Vol. 36, No. 3, 1999, pp. 475–483,
doi:10.2514/2.3469.

15. Lachaud, J. R., Martin, A., Cozmuta, I., and Laub, B., "Ablation test-case series 1," in "4th AFOSR/SNL/NASA Ablation Workshop," Albuquerque, NM, 2010.

16. Lachaud, J. R., Martin, A., van Eekelen, A., and Cozmuta, I., "Ablation test-case series 2," in "5th Ablation Workshop," Lexington, KY, AW05-051, 2012, pp. 10–18.

17. Wright, M. J., Candler, G. V., and Bose, D., "Data-Parallel Line Relaxation method for the Navier-Stokes equations," *AIAA Journal*, Vol. 36, No. 9, 1998, pp. 1603–1609, doi:10.2514/2.586.

18. Bose, D., Santos, J. A., Rodriguez, E., White, T. R., and Mahzari, M., "Mars Science Laboratory Heat Shield Instrumentation and Arc Jet Characterization," in "44th AIAA Thermophysics Conference," AIAA Paper 2013-2778, 2013, pp. 1–18, doi:10.2514/6.2013-2778.

19. Martin, A. and Boyd, I. D., "Non-Darcian behavior of pyrolysis gas in a thermal protection system," *Journal of Thermophysics and Heat Transfer*, Vol. 24, No. 1, 2010, pp. 60–68, doi:10.2514/1.44103.

20. Stackpoole, M., Sepka, S., Cozmuta, I., and Kontinos, D. A., "Post-Flight Evaluation of Stardust Sample Return Capsule Forebody Heatshield Material," in "46th AIAA Aerospace Sciences Meeting and Exhibit," Reno, NV, AIAA Paper 2008-1202, 2008, pp. 1–7, doi:10.2514/6.2008-1202.

21. Desai, P. N. and Qualls, G. D., "Stardust Entry Reconstruction," in "46th AIAA Aerospace Sciences Meeting and Exhibit," AIAA Paper 2008-1198, 2008, doi:10.2514/6.2008-1198.

22. Milos, F. and Chen, Y.-K., "Ablation, Thermal Response, and Chemistry Program for Analysis of Thermal Protection Systems," in "10th AIAA/ASME Joint Thermophysics and Heat Transfer Conference," Chicago, IL, AIAA Paper 2010-4663, 2010, doi:10.2514/6.2010-4663.

23. Trumble, K. A., Cozmuta, I., Sepka, A. S., Jenniskens, P., and Winter, M., "Postflight Aerothermal Analysis of the Stardust Sample Return Capsule," *Journal of Spacecraft and Rockets*, Vol. 47, No. 5, 2010, pp. 765–774, doi:10.2514/1.41514.

24. Edquist, K. T., Hollis, B. R., Johnston, C. O., Bose, D., White, T. R., and Mahzari, M., "Mars Science Laboratory Heatshield Aerothermodynamics: Design and Reconstruction," in "44th AIAA Thermophysics Conference," San Diego, CA, AIAA Paper 2013-2781, 2013, pp. 1–32, doi:10.2514/6.2013-2781.

25. Bose, D., White, T., Mahzari, M., and Edquist, K., "Reconstruction of Aerothermal Environment and Heat Shield Response of Mars Science Laboratory," *Journal of Spacecraft and Rockets*, Vol. 51, No. 4, 2014, pp. 1174–1184, doi:10.2514/1.A32783.

26. White, T. R., Mahzari, M., Bose, D., and Santos, J. A., "Post-flight Analysis of the Mars Science Laboratory Entry Aerothermal Environment and Thermal Protection System Response," in "44th AIAA Thermophysics Conference," San Diego, CA, AIAA Paper 2013-2779, 2013, pp. 1–19, doi:10.2514/6.2013-2779.

27. Mahzari, M., Braun, R. D., White, T. R., and Bose, D., "Inverse Estimation of the Mars Science Laboratory Entry Aerothermal Environment and Thermal Protection System Response," in "44th AIAA Thermophysics Conference," San Diego, CA, AIAA Paper 2013-2780, 2013, pp. 1–19, doi:10.2514/6.2013-2780.

Appendix A

Comparison to FIAT

The graphs presented in Fig. A8 presents the comparison of PATO and FIAT for the MSL test case for all cores, except for Core 2, which is presented in the main text.

(a) Core 1

(b) Core 3

(c) Core 4

(d) Core 5

(e) Core 6

(f) Core 7
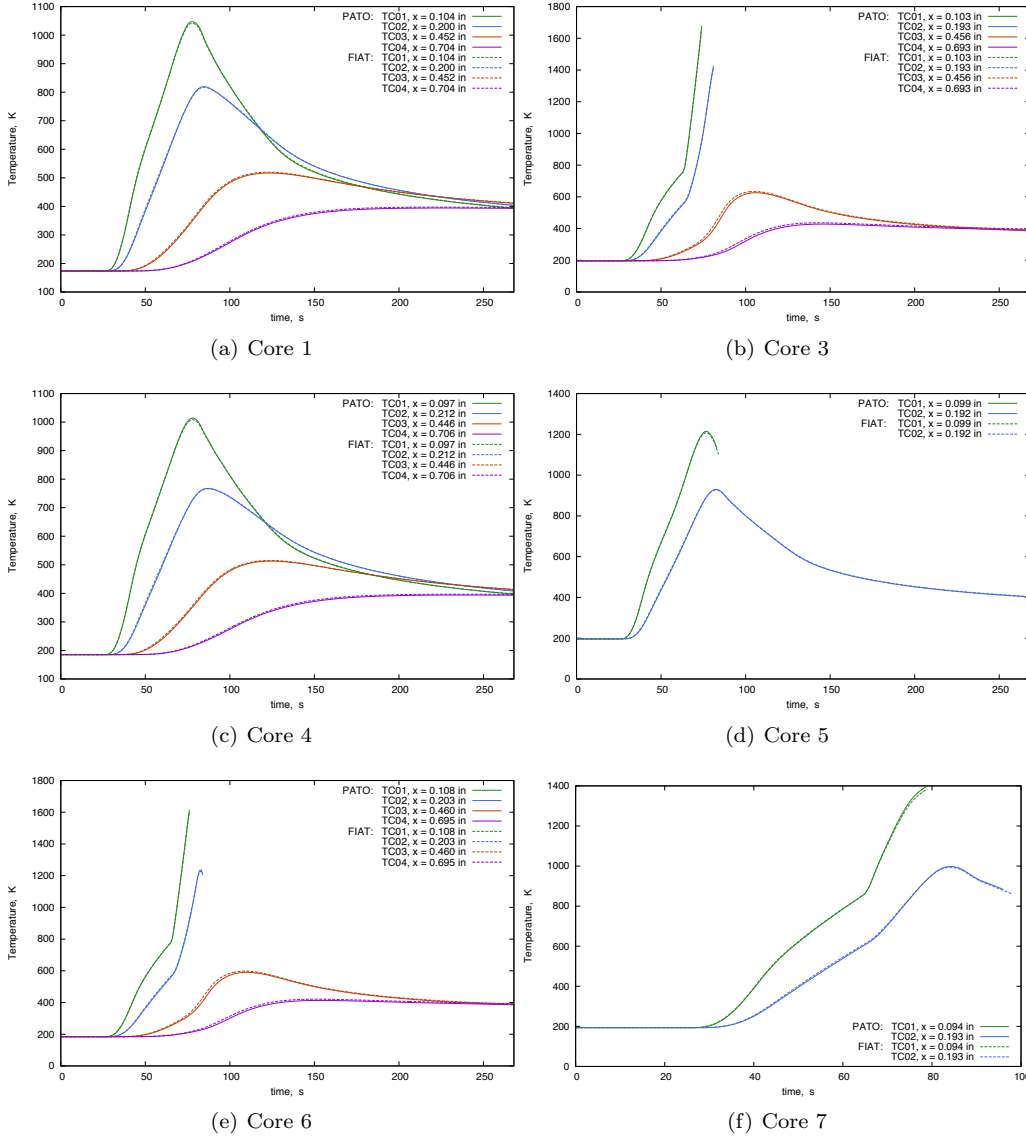
Figure A8. *Comparison of PATO and FIAT for the MEDLI cores of Mars Science Laboratory.*

Appendix B

Flight Comparison

The graphs presented in Fig. B9 presents the comparison of PATO and Flight Data measurements for the MSL test case for all cores, except for Core 2, which is presented in the main text.

(a) Core 1

(b) Core 3

(c) Core 4

(d) Core 5

(e) Core 6

(f) Core 7
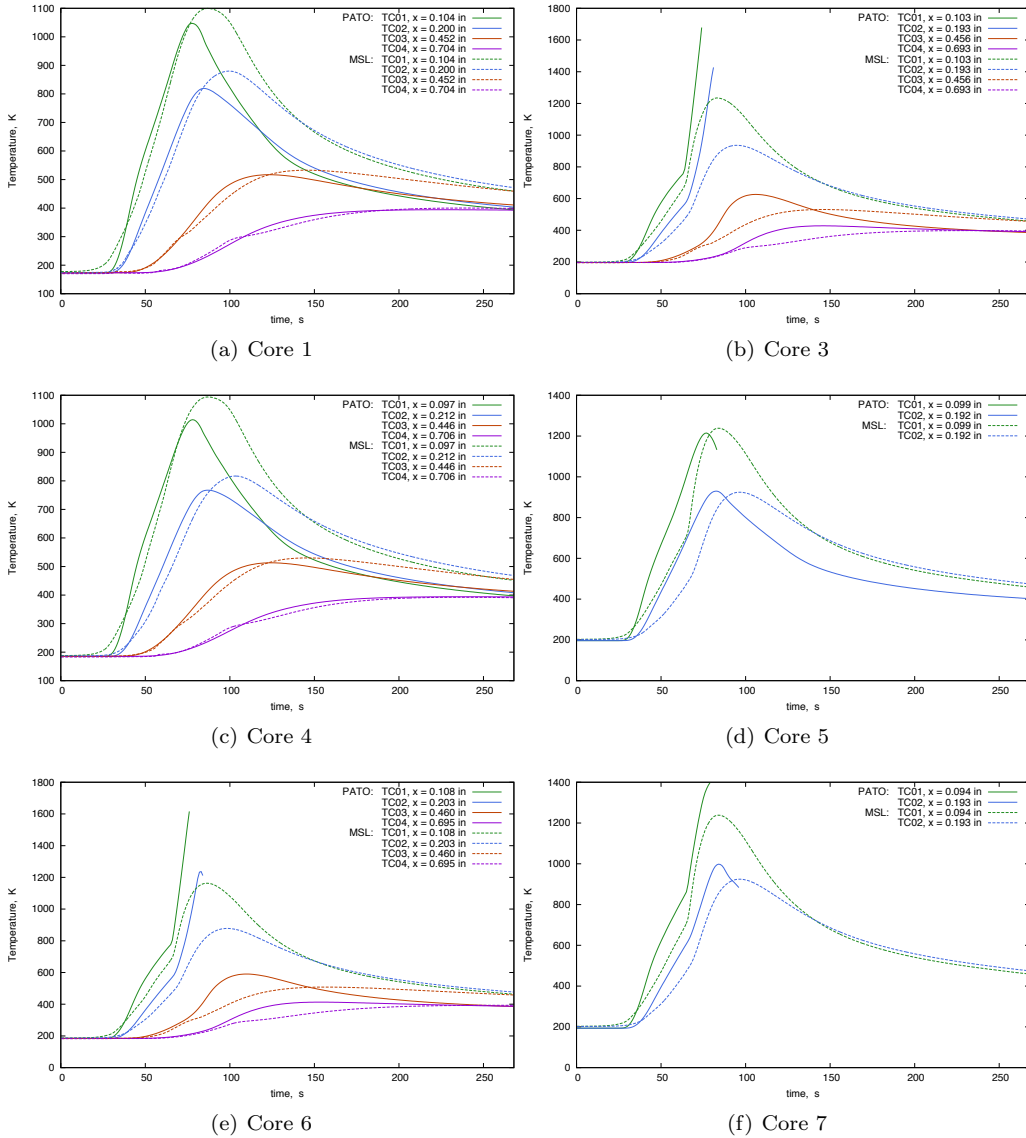
Figure B9. *Comparison of PATO and the Flight DATA for the MEDLI cores of Mars Science Laboratory.*

14

Appendix C

Thermocouple Driver

The graphs presented in Fig. C10 presents the comparison of PATO using the thermocouple 1 as the temperature driver and the MSL Flight Data, for all cores, except for Core 2, which is presented in the main text.
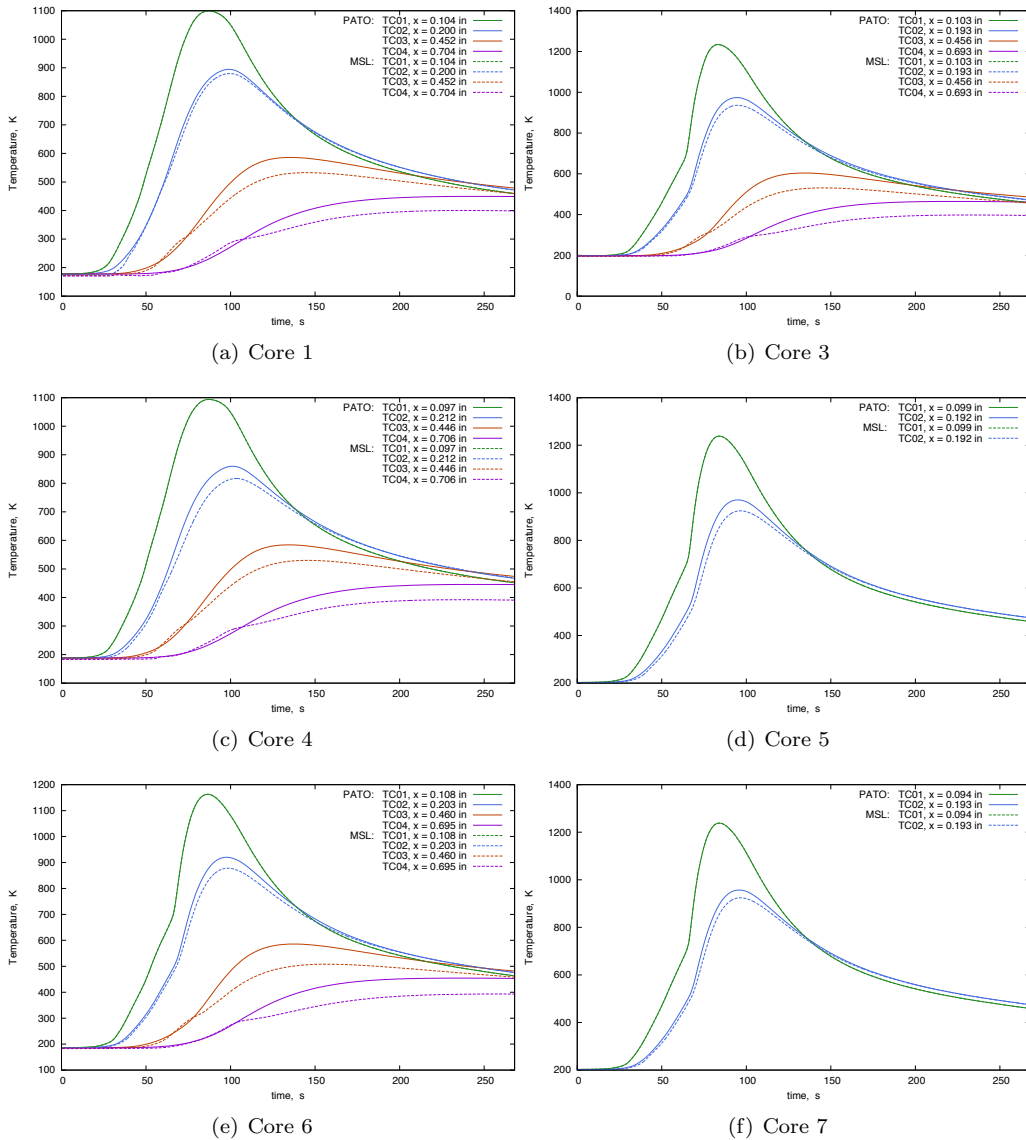
Figure C10. *Comparison of the MSL Flight DATA and PATO using the thermocouple 1 as the temperature driver, for the MEDLI cores of Mars Science Laboratory.*

Appendix D

Test Cases

This section provides boundary conditions used for the comparison studies.

Table D2. *Summary of the overall errors between the PATO and FIAT for all test cases.*

t	P	T_w	$\rho U_e C_H$	h_r	λ	T_∞
(s)	(pa)	(K)	(kg/m^2/s)	(J/kg)		(K)
0	101325	300	0.3e-2	0	0.5	300
0.1	101325	1644	0.3	1.5e6	0.5	300
60	101325	1644	0.3	1.5e6	0.5	300
60.1	101325	300	0.3e-2	0	0.5	300
120	101325	300	0.3e-2	0	0.5	300

Table D3. *Boundary conditions used for the Stardust Core 1 test case.*

t	P	$\rho U_e C_H$	h_r	λ	T_∞
(s)	(pa)	(kg/m^2/s)	(J/kg)		(K)
0	1.65787	5.067E-05	77926960.0	0.5	266.48
1	1.65787	5.072E-05	77984280.0	0.5	266.48
2	1.65787	5.078E-05	78040736.0	0.5	266.48
3	1.65787	5.083E-05	78095240.0	0.5	266.48
4	1.65787	5.088E-05	78146168.0	0.5	266.48
5	1.65787	5.092E-05	78191960.0	0.5	266.48
6	3.31586	1.019E-04	78231464.0	0.5	266.48
7	3.31586	1.019E-04	78263928.0	0.5	266.48
8	4.97374	1.530E-04	78288600.0	0.5	266.48
9	4.97374	1.531E-04	78304896.0	0.5	266.48
10	6.63172	2.041E-04	78312712.0	0.5	266.48
11	8.28960	2.552E-04	78313424.0	0.5	266.48
12	9.94758	3.062E-04	78308464.0	0.5	266.48
13	13.2634	4.082E-04	78299512.0	0.5	266.48
14	18.2374	5.612E-04	78288136.0	0.5	266.48
15	23.2105	7.140E-04	78269528.0	0.5	266.48
16	29.8422	9.176E-04	78245832.0	0.5	266.48
17	38.1326	1.171E-03	78219824.0	0.5	266.48
18	51.3960	1.578E-03	78189856.0	0.5	266.48
19	66.3172	2.035E-03	78156920.0	0.5	266.48
20	86.2123	2.644E-03	78121576.0	0.5	266.48
21	114.395	3.507E-03	78091120.0	0.5	266.48
22	147.559	4.521E-03	78064576.0	0.5	266.48
23	190.663	5.839E-03	78036672.0	0.5	266.48
24	245.368	7.509E-03	78003200.0	0.5	266.48
25	313.347	9.582E-03	77959840.0	0.5	266.48
26	396.241	1.210E-02	77907272.0	0.5	266.48
27	497.374	1.517E-02	77844248.0	0.5	266.48
28	618.406	1.882E-02	77733200.0	0.5	266.48
29	764.304	2.320E-02	77592344.0	0.5	266.48
30	938.391	2.840E-02	77434424.0	0.5	266.48
31	1145.58	3.456E-02	77258832.0	0.5	266.48
32	1407.60	4.233E-02	77100144.0	0.5	266.48
33	1724.24	5.167E-02	76914176.0	0.5	266.48
34	2120.63	5.633E-02	76695600.0	0.5	266.48
35	2516.91	6.100E-02	76431952.0	0.5	266.48
36	3068.32	6.636E-02	76099072.0	0.5	266.48
37	3619.73	7.172E-02	75713336.0	0.5	266.48
38	4377.74	7.779E-02	75265752.0	0.5	266.48
39	5135.75	8.386E-02	74754360.0	0.5	266.48
40	6131.37	9.050E-02	74189416.0	0.5	266.48
41	7127.09	9.714E-02	73526936.0	0.5	266.48
42	8386.06	0.1042	72754784.0	0.5	266.48
43	9645.12	0.1113	71859952.0	0.5	266.48
44	11163.9	0.1188	70830384.0	0.5	266.48
45	12683.8	0.1262	69361208.0	0.5	266.48
46	14432.7	0.1338	68317688.0	0.5	266.48
47	16181.6	0.1414	66516592.0	0.5	266.48
48	18102.7	0.1486	65139768.0	0.5	266.48

t	P	$\rho U_e C_H$	h_r	λ	T_∞
(s)	(pa)	(kg/m^2/s)	(J/kg)		(K)
49	20024.8	0.1559	63297544.0	0.5	266.48
50	21945.9	0.1631	61280148.0	0.5	266.48
51	23836.7	0.1695	59093460.0	0.5	266.48
52	25727.4	0.1759	56748968.0	0.5	266.48
53	27467.1	0.1814	54266944.0	0.5	266.48
54	29053.9	0.1863	51676628.0	0.5	266.48
55	30444.1	0.1902	48994492.0	0.5	266.48
56	31626.5	0.1930	46246772.0	0.5	266.48
57	32600.3	0.1947	43464944.0	0.5	266.48
58	33332.8	0.1960	40679956.0	0.5	266.48
59	33808.1	0.1969	37920332.0	0.5	266.48
60	34009.7	0.1971	35210932.0	0.5	266.48
61	33950.9	0.1965	32576506.0	0.5	266.48
62	33667.2	0.1952	30040552.0	0.5	266.48
63	33010.6	0.1924	27619866.0	0.5	266.48
64	32354.0	0.1896	25326390.0	0.5	266.48
65	31698.5	0.1867	23169220.0	0.5	266.48
66	30671.0	0.1821	21153954.0	0.5	266.48
67	29643.6	0.1775	19282284.0	0.5	266.48
68	28616.2	0.1729	17552294.0	0.5	266.48
69	27588.7	0.1683	15958944.0	0.5	266.48
70	26561.3	0.1637	14492873.0	0.5	266.48
71	25426.4	0.1583	13149026.0	0.5	266.48
72	24292.6	0.1530	11921329.0	0.5	266.48
73	23157.8	0.1476	10802757.0	0.5	266.48
74	22024.0	0.1422	9786229.00	0.5	266.48
75	20889.1	0.1368	8864601.00	0.5	266.48
76	19887.0	0.1306	8030480.50	0.5	266.48
77	18884.9	0.1244	7276327.00	0.5	266.48
78	17881.8	0.1182	6593630.00	0.5	266.48
79	16879.7	0.1120	5974079.50	0.5	266.48
80	16058.9	0.1058	5412933.50	0.5	266.48
81	15198.7	0.1028	4906979.00	0.5	266.48
82	14406.3	9.977E-02	4451572.00	0.5	266.48
83	13656.5	9.673E-02	4041513.75	0.5	266.48
84	12943.2	9.370E-02	3672258.50	0.5	266.48
85	12275.5	9.066E-02	3339807.00	0.5	266.48
86	11649.3	8.762E-02	3040593.75	0.5	266.48
87	11058.6	8.458E-02	2770945.00	0.5	266.48
88	10497.2	8.154E-02	2527848.75	0.5	266.48
89	9970.07	7.850E-02	2307711.50	0.5	266.48
90	9479.05	7.547E-02	2108659.25	0.5	266.48
91	9015.59	7.243E-02	1928025.38	0.5	266.48
92	8576.14	6.939E-02	1764369.00	0.5	266.48
93	8161.72	6.635E-02	1615863.88	0.5	266.48
94	7774.76	6.331E-02	1481035.62	0.5	266.48
95	7413.13	6.027E-02	1358598.38	0.5	266.48
96	7071.06	5.724E-02	1247165.50	0.5	266.48
97	6747.94	5.420E-02	1145727.50	0.5	266.48
98	6445.68	5.116E-02	1053437.12	0.5	266.48
99	6239.69	4.812E-02	969291.688	0.5	266.48

t	P	$\rho U_e C_H$	h_r	λ	T_∞
(s)	(pa)	(kg/m^2/s)	(J/kg)		(K)
100	6019.00	4.642E-02	892433.812	0.5	266.48
101	5806.22	4.478E-02	822151.250	0.5	266.48
102	5602.15	4.320E-02	757936.562	0.5	266.48
103	5403.86	4.167E-02	699069.250	0.5	266.48
104	5212.46	4.020E-02	644999.562	0.5	266.48
105	5028.65	3.878E-02	595337.500	0.5	266.48
106	4852.25	3.742E-02	549742.438	0.5	266.48
107	4681.51	3.610E-02	507891.656	0.5	266.48
108	4516.25	3.483E-02	469469.500	0.5	266.48
109	4357.07	3.360E-02	434179.656	0.5	266.48
110	4203.97	3.242E-02	401749.875	0.5	266.48
111	4056.24	3.128E-02	371921.219	0.5	266.48
112	3913.17	3.018E-02	344472.031	0.5	266.48
113	3774.96	2.911E-02	319206.562	0.5	266.48
114	3641.82	2.808E-02	295954.125	0.5	266.48
115	3513.44	2.709E-02	274572.031	0.5	266.48
116	3389.32	2.614E-02	254932.438	0.5	266.48
117	3269.25	2.521E-02	236908.906	0.5	266.48
118	3152.22	2.431E-02	220217.750	0.5	266.48
119	3041.57	2.345E-02	205210.156	0.5	266.48
120	2933.66	2.262E-02	191296.031	0.5	266.48
121	2829.60	2.182E-02	178495.844	0.5	266.48
122	2730.20	2.105E-02	166689.750	0.5	266.48
123	2634.34	2.031E-02	155849.734	0.5	266.48
124	2541.73	1.960E-02	145892.141	0.5	266.48
125	2452.06	1.891E-02	136743.047	0.5	266.48
126	2365.22	1.824E-02	128329.023	0.5	266.48
127	2281.33	1.759E-02	120580.742	0.5	266.48
128	2200.37	1.697E-02	113440.141	0.5	266.48
129	2122.04	1.636E-02	106857.414	0.5	266.48
130	2046.25	1.578E-02	100786.508	0.5	266.48
131	1972.79	1.521E-02	95178.4531	0.5	266.48
132	1901.97	1.466E-02	89989.8672	0.5	266.48
133	1830.33	1.411E-02	84956.8984	0.5	266.48

Table D4. *Boundary conditions used for the Stardust Core 2 test case.*

t	P	$\rho U_e C_H$	h_r	λ	T_∞
(s)	(pa)	(kg/m^2/s)	(J/kg)		(K)
0	1.42452812	3.25600122E-05	77926960.0	0.500000000	266.480011
1	1.42452812	3.25956498E-05	77984280.0	0.500000000	266.480011
2	1.42452812	3.26312875E-05	78040736.0	0.500000000	266.480011
3	1.42452812	3.26654626E-05	78095240.0	0.500000000	266.480011
4	1.42452812	3.26971931E-05	78146168.0	0.500000000	266.480011
5	1.42452812	3.27259986E-05	78191960.0	0.500000000	266.480011
6	2.84895492	6.55017939E-05	78231464.0	0.500000000	266.480011
7	2.84895492	6.55408512E-05	78263928.0	0.500000000	266.480011
8	4.27348328	9.83625359E-05	78288600.0	0.500000000	266.480011
9	4.27348328	9.83918289E-05	78304896.0	0.500000000	266.480011
10	5.69790983	1.31208624E-04	78312712.0	0.500000000	266.480011
11	7.12243795	1.64010780E-04	78313424.0	0.500000000	266.480011
12	8.54686451	1.96793408E-04	78308464.0	0.500000000	266.480011
13	11.3960228	2.62348913E-04	78299512.0	0.500000000	266.480011
14	15.6688986	3.60652863E-04	78288136.0	0.500000000	266.480011
15	19.9427853	4.58849390E-04	78269528.0	0.500000000	266.480011
16	25.6402912	5.89696749E-04	78245832.0	0.500000000	266.480011
17	32.7634392	7.53097294E-04	78219824.0	0.500000000	266.480011
18	44.1584511	1.01447955E-03	78189856.0	0.500000000	266.480011
19	56.9791031	1.30818062E-03	78156920.0	0.500000000	266.480011
20	74.0726318	1.69947313E-03	78121576.0	0.500000000	266.480011
21	98.2892990	2.25372659E-03	78091120.0	0.500000000	266.480011
22	126.777840	2.90552224E-03	78064576.0	0.500000000	266.480011
23	163.812119	3.75230494E-03	78036672.0	0.500000000	266.480011
24	210.826920	4.82595433E-03	78003200.0	0.500000000	266.480011
25	269.230652	6.15766691E-03	77959840.0	0.500000000	266.480011
26	340.451996	7.77897891E-03	77907272.0	0.500000000	266.480011
27	427.348328	9.75228380E-03	77844248.0	0.500000000	266.480011
28	531.328064	1.20995492E-02	77733200.0	0.500000000	266.480011
29	656.687378	1.49135338E-02	77592344.0	0.500000000	266.480011
30	806.253174	1.82542857E-02	77434424.0	0.500000000	266.480011
31	984.311646	2.22101696E-02	77258832.0	0.500000000	266.480011
32	1209.41516	2.72044577E-02	77100144.0	0.500000000	266.480011
33	1481.47278	3.32044326E-02	76914176.0	0.500000000	266.480011
34	1826.68713	3.67951468E-02	76695600.0	0.500000000	266.480011
35	2171.90137	4.03858572E-02	76431952.0	0.500000000	266.480011
36	2651.47266	4.43505310E-02	76099072.0	0.500000000	266.480011
37	3131.04370	4.83156890E-02	75713336.0	0.500000000	266.480011
38	3787.62988	5.25644943E-02	75265752.0	0.500000000	266.480011
39	4444.11426	5.68167157E-02	74754360.0	0.500000000	266.480011
40	5304.56641	6.11470491E-02	74189416.0	0.500000000	266.480011
41	6165.01855	6.54822662E-02	73526936.0	0.500000000	266.480011
42	7251.42480	6.97637796E-02	72754784.0	0.500000000	266.480011
43	8337.83105	7.40501732E-02	71859952.0	0.500000000	266.480011
44	9647.55859	7.81852305E-02	70830384.0	0.500000000	266.480011
45	10957.2852	8.23202804E-02	69361208.0	0.500000000	266.480011
46	12467.0273	8.62356499E-02	68317688.0	0.500000000	266.480011
47	13975.7578	9.01510119E-02	66516592.0	0.500000000	266.480011
48	15636.4746	9.36709344E-02	65139768.0	0.500000000	266.480011

t	P	$\rho U_e C_H$	h_r	λ	T_∞
(s)	(pa)	(kg/m^2/s)	(J/kg)		(K)
49	17298.2031	9.71859694E-02	63297544.0	0.500000000	266.480011
50	18958.9219	0.100705892	61280148.0	0.500000000	266.480011
51	20582.1484	0.103576511	59093460.0	0.500000000	266.480011
52	22206.3867	0.106442243	56748968.0	0.500000000	266.480011
53	23697.8906	0.108834423	54266944.0	0.500000000	266.480011
54	25075.9121	0.110855572	51676628.0	0.500000000	266.480011
55	26307.0098	0.112447105	48994492.0	0.500000000	266.480011
56	27329.3770	0.113360040	46246772.0	0.500000000	266.480011
57	28152.1367	0.113540672	43464944.0	0.500000000	266.480011
58	28768.1934	0.113115937	40679956.0	0.500000000	266.480011
59	29170.4531	0.112173714	37920332.0	0.500000000	266.480011
60	29360.9453	0.110855572	35210932.0	0.500000000	266.480011
61	29340.6797	0.109161526	32576506.0	0.500000000	266.480011
62	29147.1504	0.107184313	30040552.0	0.500000000	266.480011
63	28628.3652	0.104513854	27619866.0	0.500000000	266.480011
64	28109.5820	0.101838514	25326390.0	0.500000000	266.480011
65	27589.7832	9.91680697E-02	23169220.0	0.500000000	266.480011
66	26764.9980	9.59117711E-02	21153954.0	0.500000000	266.480011
67	25939.2012	9.26603600E-02	19282284.0	0.500000000	266.480011
68	25113.4004	8.94040689E-02	17552294.0	0.500000000	266.480011
69	24287.6035	8.61526504E-02	15958944.0	0.500000000	266.480011
70	23461.8027	8.28963593E-02	14492873.0	0.500000000	266.480011
71	22512.3887	7.98109397E-02	13149026.0	0.500000000	266.480011
72	21562.9727	7.67255127E-02	11921329.0	0.500000000	266.480011
73	20612.5449	7.36400858E-02	10802757.0	0.500000000	266.480011
74	19663.1289	7.05497786E-02	9786229.00	0.500000000	266.480011
75	18713.7148	6.74643591E-02	8864601.00	0.500000000	266.480011
76	17928.4453	6.41397163E-02	8030480.50	0.500000000	266.480011
77	17143.1777	6.08101897E-02	7276327.00	0.500000000	266.480011
78	16358.9209	5.74855506E-02	6593630.00	0.500000000	266.480011
79	15573.6523	5.41609079E-02	5974079.50	0.500000000	266.480011
80	14386.1240	5.08313850E-02	5412933.50	0.500000000	266.480011
81	13615.0400	4.95767072E-02	4906979.00	0.500000000	266.480011
82	12905.7656	4.83195968E-02	4451572.00	0.500000000	266.480011
83	12233.9805	4.70629707E-02	4041513.75	0.500000000	266.480011
84	11595.6328	4.58068289E-02	3672258.50	0.500000000	266.480011
85	10996.8018	4.45506908E-02	3339807.00	0.500000000	266.480011
86	10436.4746	4.32940647E-02	3040593.75	0.500000000	266.480011
87	9906.44434	4.20379266E-02	2770945.00	0.500000000	266.480011
88	9404.27734	4.07817848E-02	2527848.75	0.500000000	266.480011
89	8931.59570	3.95256504E-02	2307711.50	0.500000000	266.480011
90	8491.74414	3.82690206E-02	2108659.25	0.500000000	266.480011
91	8076.51465	3.70128825E-02	1928025.38	0.500000000	266.480011
92	7682.86670	3.57567444E-02	1764369.00	0.500000000	266.480011
93	7311.61182	3.45001146E-02	1615863.88	0.500000000	266.480011
94	6964.97900	3.32439803E-02	1481035.62	0.500000000	266.480011
95	6640.94189	3.19878384E-02	1358598.38	0.500000000	266.480011
96	6334.53516	3.07312123E-02	1247165.50	0.500000000	266.480011
97	6045.04932	2.94750761E-02	1145727.50	0.500000000	266.480011
98	5774.30908	2.82189362E-02	1053437.12	0.500000000	266.480011
99	5600.84082	2.69627962E-02	969291.688	0.500000000	266.480011

t	P	$\rho U_e C_H$	h_r	λ	T_∞
(s)	(pa)	(kg/m^2/s)	(J/kg)		(K)
100	5402.64941	2.60088537E-02	892433.812	0.500000000	266.480011
101	5211.65137	2.50890851E-02	822151.250	0.500000000	266.480011
102	5028.45557	2.42073983E-02	757936.562	0.500000000	266.480011
103	4850.52930	2.33506057E-02	699069.250	0.500000000	266.480011
104	4678.68164	2.25235969E-02	644999.562	0.500000000	266.480011
105	4513.72461	2.17297822E-02	595337.500	0.500000000	266.480011
106	4355.35400	2.09667254E-02	549742.438	0.500000000	266.480011
107	4202.15039	2.02295426E-02	507891.656	0.500000000	266.480011
108	4053.81079	1.95153058E-02	469469.500	0.500000000	266.480011
109	3910.84082	1.88274328E-02	434179.656	0.500000000	266.480011
110	3773.54565	1.81659218E-02	401749.875	0.500000000	266.480011
111	3640.91113	1.75273567E-02	371921.219	0.500000000	266.480011
112	3512.43115	1.69092957E-02	344472.031	0.500000000	266.480011
113	3388.40918	1.63117386E-02	319206.562	0.500000000	266.480011
114	3268.94727	1.57366395E-02	295954.125	0.500000000	266.480011
115	3153.74048	1.51820434E-02	274572.031	0.500000000	266.480011
116	3042.28320	1.46455113E-02	254932.438	0.500000000	266.480011
117	2934.47314	1.41265551E-02	236908.906	0.500000000	266.480011
118	2829.39917	1.36212679E-02	220217.750	0.500000000	266.480011
119	2730.20215	1.31433206E-02	205210.156	0.500000000	266.480011
120	2633.23413	1.26766013E-02	191296.031	0.500000000	266.480011
121	2539.91382	1.22269690E-02	178495.844	0.500000000	266.480011
122	2450.64648	1.17978407E-02	166689.750	0.500000000	266.480011
123	2364.62134	1.13833593E-02	155849.734	0.500000000	266.480011
124	2281.43359	1.09830350E-02	145892.141	0.500000000	266.480011
125	2200.98169	1.05954055E-02	136743.047	0.500000000	266.480011
126	2122.96143	1.02204671E-02	128329.023	0.500000000	266.480011
127	2047.77820	9.85773467E-03	120580.742	0.500000000	266.480011
128	1975.02698	9.50818323E-03	113440.141	0.500000000	266.480011
129	1904.80859	9.16986074E-03	106857.414	0.500000000	266.480011
130	1836.71826	8.84227827E-03	100786.508	0.500000000	266.480011
131	1770.75574	8.52446072E-03	95178.4531	0.500000000	266.480011
132	1707.22498	8.21884722E-03	89989.8672	0.500000000	266.480011
133	1642.98486	7.90932775E-03	84956.8984	0.500000000	266.480011

Table D5. *Boundary conditions used for the Mars Science Laboratory MISP 2 test case.*

t (s)	Recovery Enthalpy (btu/lb)	Radiative Heating (btu/ft2-s)	Heat Transfer Coefficient (lb/ft2-s)	Pressure (atm)	λ
0.000	3506.61	0.00	2.04E-8	1.52E-7	0.50
1.000	3509.01	0.00	2.04E-8	1.52E-7	0.50
2.000	3511.40	0.00	2.04E-8	1.52E-7	0.50
3.000	3513.79	0.00	2.04E-8	1.52E-7	0.50
4.000	3516.17	0.00	2.04E-8	1.52E-7	0.50
5.000	3518.54	0.00	2.04E-8	1.52E-7	0.50
6.000	3520.90	0.00	2.04E-8	1.52E-7	0.50
7.000	3523.26	0.00	2.04E-8	1.52E-7	0.50
8.000	3525.61	0.00	2.04E-8	1.52E-7	0.50
9.000	3527.95	0.00	2.04E-8	1.52E-7	0.50
10.00	3530.28	0.00	2.04E-8	1.52E-7	0.50
11.00	3532.60	0.00	2.04E-8	1.52E-7	0.50
12.00	3534.92	0.00	2.04E-8	1.52E-7	0.50
13.00	3537.22	0.00	2.04E-8	1.52E-7	0.50
14.00	3539.52	0.00	2.04E-8	1.52E-7	0.50
15.00	3541.80	0.00	2.04E-8	1.52E-7	0.50
16.00	3544.07	0.00	2.04E-8	1.52E-7	0.50
17.00	3546.33	0.00	2.04E-8	1.52E-7	0.50
18.00	3548.58	0.00	2.04E-8	1.52E-7	0.50
19.00	3550.81	0.00	2.04E-8	1.52E-7	0.50
20.00	3553.03	0.00	2.04E-8	1.52E-7	0.50
21.00	3555.24	0.00	2.04E-8	1.52E-7	0.50
22.00	3557.40	0.00	2.04E-8	1.52E-7	0.50
23.00	3559.57	0.00	2.04E-8	1.52E-7	0.50
24.00	3561.71	0.00	2.04E-8	1.52E-7	0.50
25.00	3563.82	0.00	2.04E-8	1.52E-7	0.50
26.00	3565.89	0.00	4.17E-6	1.90E-5	0.50
27.00	3567.93	0.00	1.63E-5	7.54E-5	0.50
28.00	3569.93	0.00	3.62E-5	1.69E-4	0.50
29.00	3571.86	0.00	6.32E-5	3.00E-4	0.50
30.00	3573.69	0.00	9.71E-5	4.69E-4	0.50
31.00	3575.39	0.00	1.37E-4	6.75E-4	0.50
32.00	3576.94	0.00	1.83E-4	9.17E-4	0.50
33.00	3578.28	0.00	2.35E-4	1.19E-3	0.50
34.00	3579.39	0.00	2.92E-4	1.51E-3	0.50
35.00	3580.22	0.00	3.54E-4	1.86E-3	0.50
36.00	3580.74	0.00	4.20E-4	2.25E-3	0.50
37.00	3580.86	0.00	4.90E-4	2.68E-3	0.50
38.00	3580.52	0.00	5.64E-4	3.14E-3	0.50
39.00	3579.71	0.00	6.41E-4	3.64E-3	0.50
40.00	3578.36	0.00	7.21E-4	4.17E-3	0.50
41.00	3576.38	0.00	8.02E-4	4.74E-3	0.50
42.00	3573.68	0.00	8.86E-4	5.34E-3	0.50
43.00	3570.06	0.00	9.72E-4	5.98E-3	0.50
44.00	3565.38	0.00	1.05E-3	6.66E-3	0.50
45.00	3559.43	0.00	1.14E-3	7.37E-3	0.50
46.00	3551.62	0.00	1.23E-3	8.12E-3	0.50
47.00	3543.06	0.00	1.32E-3	8.90E-3	0.50
48.00	3532.92	0.00	1.40E-3	9.72E-3	0.50

t (s)	Recovery Enthalpy (btu/lb)	Radiative Heating (btu/ft2-s)	Heat Transfer Coefficient (lb/ft2-s)	Pressure (atm)	λ
49.00	3521.02	0.00	1.49E-3	1.05E-2	0.50
50.00	3507.12	0.00	1.59E-3	1.19E-2	0.50
51.00	3491.37	0.00	1.72E-3	1.40E-2	0.50
52.00	3472.83	0.00	1.81E-3	1.65E-2	0.50
53.00	3450.05	0.00	1.86E-3	1.90E-2	0.50
54.00	3423.61	0.00	1.89E-3	2.19E-2	0.50
55.00	3392.42	0.00	1.94E-3	2.52E-2	0.50
56.00	3356.11	0.00	2.03E-3	2.90E-2	0.50
57.00	3314.52	0.00	2.18E-3	3.38E-2	0.50
58.00	3267.21	0.00	2.28E-3	3.85E-2	0.50
59.00	3213.86	0.00	2.36E-3	4.34E-2	0.50
60.00	3153.56	0.00	2.44E-3	4.87E-2	0.50
61.00	3084.46	0.00	2.52E-3	5.44E-2	0.50
62.00	3006.10	0.00	2.60E-3	6.09E-2	0.50
63.00	2917.87	0.00	2.69E-3	6.85E-2	0.50
64.00	2819.53	0.00	2.77E-3	7.68E-2	0.50
65.00	2710.25	0.00	1.53E-2	8.64E-2	0.29
66.00	2589.67	0.00	1.66E-2	9.57E-2	0.29
67.00	2457.58	0.00	1.79E-2	0.10	0.29
68.00	2314.67	0.00	1.91E-2	0.11	0.29
69.00	2160.91	0.00	2.03E-2	0.12	0.29
70.00	1996.46	0.00	2.15E-2	0.13	0.29
71.00	1821.02	0.00	2.27E-2	0.14	0.29
72.00	1636.09	0.00	2.39E-2	0.15	0.29
73.00	1441.42	0.00	2.52E-2	0.16	0.29
74.00	1236.02	0.00	2.67E-2	0.17	0.29
75.00	1022.11	0.00	2.83E-2	0.18	0.29
76.00	805.170	0.00	2.92E-2	0.19	0.29
77.00	586.658	0.00	2.98E-2	0.19	0.29
78.00	367.375	0.00	3.04E-2	0.20	0.29
79.00	148.771	0.00	3.09E-2	0.20	0.29
80.00	-67.4520	0.00	3.13E-2	0.21	0.29
81.00	-279.152	0.00	3.12E-2	0.21	0.29
82.00	-483.904	0.00	3.03E-2	0.20	0.29
83.00	-681.505	0.00	2.89E-2	0.20	0.29
84.00	-871.671	0.00	2.72E-2	0.20	0.29
85.00	-1053.02	0.00	2.57E-2	0.20	0.29
86.00	-1224.92	0.00	2.39E-2	0.19	0.29
87.00	-1386.74	0.00	2.19E-2	0.19	0.29
88.00	-1538.89	0.00	1.98E-2	0.18	0.29
89.00	-1682.14	0.00	1.79E-2	0.18	0.29
90.00	-1816.51	0.00	1.64E-2	0.17	0.29
91.00	-1941.97	0.00	1.55E-2	0.16	0.29
92.00	-2058.72	0.00	1.47E-2	0.16	0.29
93.00	-2167.32	0.00	1.41E-2	0.15	0.29
94.00	-2268.43	0.00	1.36E-2	0.14	0.29
95.00	-2362.57	0.00	1.31E-2	0.14	0.29
96.00	-2450.18	0.00	1.25E-2	0.13	0.29
97.00	-2531.59	0.00	1.21E-2	0.13	0.29
98.00	-2607.10	0.00	1.16E-2	0.12	0.29
99.00	-2677.02	0.00	1.11E-2	0.12	0.29

t	Recovery Enthalpy	Radiative Heating	Heat Transfer Coefficient	Pressure	λ
(s)	(btu/lb)	(btu/ft2-s)	(lb/ft2-s)	(atm)	
100.0	-2741.80	0.00	1.06E-2	0.114	0.29
101.0	-2801.93	0.00	1.01E-2	0.109	0.29
102.0	-2857.70	0.00	9.68E-3	0.104	0.29
103.0	-2909.43	0.00	9.20E-3	9.92E-2	0.29
104.0	-2957.39	0.00	8.74E-3	9.46E-2	0.29
105.0	-3001.96	0.00	8.29E-3	9.03E-2	0.29
106.0	-3043.49	0.00	7.85E-3	8.63E-2	0.29
107.0	-3082.21	0.00	7.42E-3	8.25E-2	0.29
108.0	-3118.23	0.00	6.99E-3	7.89E-2	0.29
109.0	-3151.87	0.00	6.59E-3	7.56E-2	0.29
110.0	-3183.40	0.00	6.22E-3	7.24E-2	0.29
111.0	-3212.87	0.00	5.90E-3	6.95E-2	0.29
112.0	-3240.47	0.00	5.61E-3	6.67E-2	0.29
113.0	-3266.40	0.00	5.32E-3	6.39E-2	0.29
114.0	-3290.66	0.00	5.03E-3	6.10E-2	0.29
115.0	-3313.47	0.00	4.73E-3	5.81E-2	0.29
116.0	-3334.95	0.00	4.44E-3	5.51E-2	0.29
117.0	-3355.08	0.00	4.15E-3	5.22E-2	0.29
118.0	-3374.11	0.00	3.87E-3	4.93E-2	0.29
119.0	-3392.00	0.00	3.59E-3	4.64E-2	0.29
120.0	-3408.90	0.00	3.31E-3	4.35E-2	0.29
121.0	-3424.86	0.00	3.03E-3	4.06E-2	0.29
122.0	-3439.92	0.00	2.77E-3	3.78E-2	0.29
123.0	-3454.19	0.00	2.51E-3	3.51E-2	0.29
124.0	-3467.65	0.00	2.26E-3	3.24E-2	0.29
125.0	-3480.46	0.00	2.01E-3	2.99E-2	0.29
126.0	-3492.58	0.00	1.78E-3	2.74E-2	0.29
127.0	-3504.12	0.00	1.56E-3	2.50E-2	0.29
128.0	-3515.09	0.00	1.35E-3	2.27E-2	0.29
129.0	-3525.57	0.00	1.15E-3	2.05E-2	0.29
130.0	-3535.55	0.00	9.67E-4	1.85E-2	0.29
131.0	-3545.01	0.00	7.94E-4	1.66E-2	0.29
132.0	-3554.07	0.00	6.36E-4	1.49E-2	0.29
133.0	-3562.63	0.00	4.94E-4	1.33E-2	0.29
134.0	-3570.88	0.00	3.68E-4	1.19E-2	0.29
135.0	-3578.72	0.00	2.59E-4	1.07E-2	0.29
136.0	-3586.24	0.00	1.68E-4	9.76E-3	0.29
137.0	-3593.39	0.00	9.58E-5	8.96E-3	0.29
138.0	-3600.23	0.00	4.31E-5	8.37E-3	0.29
139.0	-3606.80	0.00	1.09E-5	8.01E-3	0.29
140.0	-3613.04	0.00	2.04E-8	7.89E-3	0.29
141.0	-3619.06	0.00	2.04E-8	7.89E-3	0.29
142.0	-3624.85	0.00	2.04E-8	7.89E-3	0.29
143.0	-3630.39	0.00	2.04E-8	7.89E-3	0.29
144.0	-3635.75	0.00	2.04E-8	7.89E-3	0.29
145.0	-3640.86	0.00	2.04E-8	7.89E-3	0.29
146.0	-3645.77	0.00	2.04E-8	7.89E-3	0.29
147.0	-3650.53	0.00	2.04E-8	7.89E-3	0.29
148.0	-3655.08	0.00	2.04E-8	7.89E-3	0.29
149.0	-3659.46	0.00	2.04E-8	7.89E-3	0.29
150.0	-3663.72	0.00	2.04E-8	7.89E-3	0.29

t (s)	Recovery Enthalpy (btu/lb)	Radiative Heating (btu/ft2-s)	Heat Transfer Coefficient (lb/ft2-s)	Pressure (atm)	λ
151.0	-3667.79	0.00	2.04E-8	7.89E-3	0.29
152.0	-3671.73	0.00	2.04E-8	7.89E-3	0.29
153.0	-3675.56	0.00	2.04E-8	7.89E-3	0.29
154.0	-3679.22	0.00	2.04E-8	7.89E-3	0.29
155.0	-3682.72	0.00	2.04E-8	7.89E-3	0.29
156.0	-3686.16	0.00	2.04E-8	7.89E-3	0.29
157.0	-3689.48	0.00	2.04E-8	7.89E-3	0.29
158.0	-3692.64	0.00	2.04E-8	7.89E-3	0.29
159.0	-3695.73	0.00	2.04E-8	7.89E-3	0.29
160.0	-3698.75	0.00	2.04E-8	7.89E-3	0.29
161.0	-3701.64	0.00	2.04E-8	7.89E-3	0.29
162.0	-3704.41	0.00	2.04E-8	7.89E-3	0.29
163.0	-3707.14	0.00	2.04E-8	7.89E-3	0.29
164.0	-3709.80	0.00	2.04E-8	7.89E-3	0.29
165.0	-3712.34	0.00	2.04E-8	7.89E-3	0.29
166.0	-3714.81	0.00	2.04E-8	7.89E-3	0.29
167.0	-3717.23	0.00	2.04E-8	7.89E-3	0.29
168.0	-3719.59	0.00	2.04E-8	7.89E-3	0.29
169.0	-3721.86	0.00	2.04E-8	7.89E-3	0.29
170.0	-3724.07	0.00	2.04E-8	7.89E-3	0.29
171.0	-3726.22	0.00	2.04E-8	7.89E-3	0.29
172.0	-3728.32	0.00	2.04E-8	7.89E-3	0.29
173.0	-3730.35	0.00	2.04E-8	7.89E-3	0.29
174.0	-3732.32	0.00	2.04E-8	7.89E-3	0.29
175.0	-3734.25	0.00	2.04E-8	7.89E-3	0.29
176.0	-3736.13	0.00	2.04E-8	7.89E-3	0.29
177.0	-3737.95	0.00	2.04E-8	7.89E-3	0.29
178.0	-3739.71	0.00	2.04E-8	7.89E-3	0.29
179.0	-3741.44	0.00	2.04E-8	7.89E-3	0.29
180.0	-3743.13	0.00	2.04E-8	7.89E-3	0.29
181.0	-3744.78	0.00	2.04E-8	7.89E-3	0.29
182.0	-3746.37	0.00	2.04E-8	7.89E-3	0.29
183.0	-3747.93	0.00	2.04E-8	7.89E-3	0.29
184.0	-3749.46	0.00	2.04E-8	7.89E-3	0.29
185.0	-3750.95	0.00	2.04E-8	7.89E-3	0.29
186.0	-3752.41	0.00	2.04E-8	7.89E-3	0.29
187.0	-3753.82	0.00	2.04E-8	7.89E-3	0.29
188.0	-3755.20	0.00	2.04E-8	7.89E-3	0.29
189.0	-3756.56	0.00	2.04E-8	7.89E-3	0.29
190.0	-3757.89	0.00	2.04E-8	7.89E-3	0.29
191.0	-3759.18	0.00	2.04E-8	7.89E-3	0.29
192.0	-3760.44	0.00	2.04E-8	7.89E-3	0.29
193.0	-3761.68	0.00	2.04E-8	7.89E-3	0.29
194.0	-3762.90	0.00	2.04E-8	7.89E-3	0.29
195.0	-3764.09	0.00	2.04E-8	7.89E-3	0.29
196.0	-3765.25	0.00	2.04E-8	7.89E-3	0.29
197.0	-3766.37	0.00	2.04E-8	7.89E-3	0.29
198.0	-3767.47	0.00	2.04E-8	7.89E-3	0.29
199.0	-3768.56	0.00	2.04E-8	7.89E-3	0.29
200.0	-3769.63	0.00	2.04E-8	7.89E-3	0.29

t	Recovery Enthalpy	Radiative Heating	Heat Transfer Coefficient	Pressure	λ
(s)	(btu/lb)	(btu/ft2-s)	(lb/ft2-s)	(atm)	
201.0	-3770.68	0.00	2.04E-8	7.89E-3	0.29
202.0	-3771.69	0.00	2.04E-8	7.89E-3	0.29
203.0	-3772.68	0.00	2.04E-8	7.89E-3	0.29
204.0	-3773.66	0.00	2.04E-8	7.89E-3	0.29
205.0	-3774.62	0.00	2.04E-8	7.89E-3	0.29
206.0	-3775.57	0.00	2.04E-8	7.89E-3	0.29
207.0	-3776.50	0.00	2.04E-8	7.89E-3	0.29
208.0	-3777.39	0.00	2.04E-8	7.89E-3	0.29
209.0	-3778.26	0.00	2.04E-8	7.89E-3	0.29
210.0	-3779.12	0.00	2.04E-8	7.89E-3	0.29
211.0	-3779.98	0.00	2.04E-8	7.89E-3	0.29
212.0	-3780.82	0.00	2.04E-8	7.89E-3	0.29
213.0	-3781.64	0.00	2.04E-8	7.89E-3	0.29
214.0	-3782.43	0.00	2.04E-8	7.89E-3	0.29
215.0	-3783.20	0.00	2.04E-8	7.89E-3	0.29
216.0	-3783.97	0.00	2.04E-8	7.89E-3	0.29
217.0	-3784.74	0.00	2.04E-8	7.89E-3	0.29
218.0	-3785.49	0.00	2.04E-8	7.89E-3	0.29
219.0	-3786.22	0.00	2.04E-8	7.89E-3	0.29
220.0	-3786.93	0.00	2.04E-8	7.89E-3	0.29
221.0	-3787.62	0.00	2.04E-8	7.89E-3	0.29
222.0	-3788.30	0.00	2.04E-8	7.89E-3	0.29
223.0	-3788.98	0.00	2.04E-8	7.89E-3	0.29
224.0	-3789.64	0.00	2.04E-8	7.89E-3	0.29
225.0	-3790.30	0.00	2.04E-8	7.89E-3	0.29
226.0	-3790.93	0.00	2.04E-8	7.89E-3	0.29
227.0	-3791.54	0.00	2.04E-8	7.89E-3	0.29
228.0	-3792.14	0.00	2.04E-8	7.89E-3	0.29
229.0	-3792.73	0.00	2.04E-8	7.89E-3	0.29
230.0	-3793.32	0.00	2.04E-8	7.89E-3	0.29
231.0	-3793.90	0.00	2.04E-8	7.89E-3	0.29
232.0	-3794.47	0.00	2.04E-8	7.89E-3	0.29
233.0	-3795.03	0.00	2.04E-8	7.89E-3	0.29
234.0	-3795.57	0.00	2.04E-8	7.89E-3	0.29
235.0	-3796.09	0.00	2.04E-8	7.89E-3	0.29
236.0	-3796.62	0.00	2.04E-8	7.89E-3	0.29
237.0	-3797.14	0.00	2.04E-8	7.89E-3	0.29
238.0	-3797.65	0.00	2.04E-8	7.89E-3	0.29
239.0	-3798.15	0.00	2.04E-8	7.89E-3	0.29
240.0	-3798.63	0.00	2.04E-8	7.89E-3	0.29
241.0	-3799.10	0.00	2.04E-8	7.89E-3	0.29
242.0	-3799.53	0.00	2.04E-8	7.89E-3	0.29
243.0	-3799.99	0.00	2.04E-8	7.89E-3	0.29
244.0	-3800.47	0.00	2.04E-8	7.89E-3	0.29
245.0	-3800.95	0.00	2.04E-8	7.89E-3	0.29
246.0	-3801.45	0.00	2.04E-8	7.89E-3	0.29
247.0	-3801.94	0.00	2.04E-8	7.89E-3	0.29
248.0	-3802.42	0.00	2.04E-8	7.89E-3	0.29
249.0	-3802.90	0.00	2.04E-8	7.89E-3	0.29
250.0	-3803.37	0.00	2.04E-8	7.89E-3	0.29

t	Recovery Enthalpy	Radiative Heating	Heat Transfer Coefficient	Pressure	λ
(s)	(btu/lb)	(btu/ft2-s)	(lb/ft2-s)	(atm)	
251.0	-3803.84	0.00	2.04E-8	7.89E-3	0.29
252.0	-3804.29	0.00	2.04E-8	7.89E-3	0.29
253.0	-3804.75	0.00	2.04E-8	7.89E-3	0.29
254.0	-3805.20	0.00	2.04E-8	7.89E-3	0.29
255.0	-3805.67	0.00	2.04E-8	7.89E-3	0.29
256.0	-3806.13	0.00	2.04E-8	7.89E-3	0.29
257.0	-3806.57	0.00	2.04E-8	7.89E-3	0.29
258.0	-3807.01	0.00	2.04E-8	7.89E-3	0.29
259.0	-3807.45	0.00	2.04E-8	7.89E-3	0.29
260.0	-3807.48	0.00	2.04E-8	7.89E-3	0.29
261.0	-3807.48	0.00	2.04E-8	7.89E-3	0.29
262.0	-3807.48	0.00	2.04E-8	7.89E-3	0.29
263.0	-3807.48	0.00	2.04E-8	7.89E-3	0.29
264.0	-3807.48	0.00	2.04E-8	7.89E-3	0.29
265.0	-3807.48	0.00	2.04E-8	7.89E-3	0.29
266.0	-3807.48	0.00	2.04E-8	7.89E-3	0.29
267.0	-3807.48	0.00	2.04E-8	7.89E-3	0.29
268.0	-3807.48	0.00	2.04E-8	7.89E-3	0.29

1. REPORT DATE (DD-MM-YYYY)	2. REPORT TYPE	3. DATES COVERED (From - To)
01-06-2015	Contractor Report	12/2013–11/2014

4. TITLE AND SUBTITLE	5a. CONTRACT NUMBER
Code-to-Code Comparison, and Material Response Modeling of Stardust and MSL using PATO and FIAT	
	5b. GRANT NUMBER
	NNX14AC93A
	5c. PROGRAM ELEMENT NUMBER

6. AUTHOR(S)	5d. PROJECT NUMBER
Ali D. Omidy, Francesco Panerai, Alexandre Martin, Jean R. Lachaud, Ioana Cozmuta, Nagi N. Mansour	
	5e. TASK NUMBER
	5f. WORK UNIT NUMBER

7. PERFORMING ORGANIZATION NAME(S) AND ADDRESS(ES)	8. PERFORMING ORGANIZATION REPORT NUMBER
NASA Ames Research Center Moffett Field, California 94035	L–

9. SPONSORING/MONITORING AGENCY NAME(S) AND ADDRESS(ES)	10. SPONSOR/MONITOR'S ACRONYM(S)
National Aeronautics and Space Administration Washington, DC 20546-0001	NASA
	11. SPONSOR/MONITOR'S REPORT NUMBER(S)
	NASA/CR–2015–218960

12. DISTRIBUTION/AVAILABILITY STATEMENT
Unclassified-Unlimited Subject Category 34 Availability: NASA STI Program (757) 864-9658

13. SUPPLEMENTARY NOTES
An electronic version can be found at http://ntrs.nasa.gov.

14. ABSTRACT

This report provides a code-to-code comparison between PATO, a recently developed high fidelity material response code, and FIAT, NASA's legacy code for ablation response modeling. The goal is to demonstrates that FIAT and PATO generate the same results when using the same models. Test cases of increasing complexity are used, from both arc-jet testing and flight experiment. When using the exact same physical models, material properties and boundary conditions, the two codes give results that are within 2% of errors. The minor discrepancy is attributed to the inclusion of the gas phase heat capacity (c_p) in the energy equation in PATO, and not in FIAT.

15. SUBJECT TERMS
Ablation, Material response, PICA; Thermal protection system; Stardust; Mars Science Laboratory

16. SECURITY CLASSIFICATION OF:			17. LIMITATION OF ABSTRACT	18. NUMBER OF PAGES	19a. NAME OF RESPONSIBLE PERSON
a. REPORT	b. ABSTRACT	c. THIS PAGE			STI Information Desk (email: help@sti.nasa.gov)
U	U	U	UU	36	19b. TELEPHONE NUMBER (Include area code) (757) 864-9658